PHYSICAL REVIEW D VOLUME 51, NUMBER 9 1 MAY 1995

Heavy-quark production by polarized and unpolarized photons in next-to-leading order

B. Kamal and Z. Merebashvili*
Department of Physics, McGill University, Montreal, Quebec, Canada H3A 2T8

A.P. Contogouris
Department of Physics, McGill University, Montreal, Quebec, Canada H3A 2T8
and Nuclear and Particle Physics, University of Athens, Athens 15771, Greece

(Received 10 January 1995)

Complete analytical results for the production of heavy-quark pairs by polarized and unpolarized photons in next-to-leading order are presented. Two-, three-, and two-plus-three-jet cross sections for a total photon spin $J_z = 0, \pm 2$ are presented for $b\bar{b}(g)$ production. The two-jet cross sections are considered as a background to $\gamma\gamma \to H^* \to b\bar{b}$ (standard model). Top-quark production, not too far above threshold, is also considered for $J_z = 0, \pm 2$. For both b- and t-quark production, the higher order QCD corrections are found to be significant.

PACS number(s): 13.65.+i, 13.88.+e, 14.65.−q, 14.70.Bh

I. INTRODUCTION

Higher (next-to-leading) order corrections (HOC's) for heavy-quark (Q,$\overline{Q}$) production in unpolarized particle collisions have been determined in detail [1–3]. For polarized particle collisions, however, analytical results were still absent. Even for the unpolarized case, only virtual + soft corrections have been presented analytically [2]. Apart from general reasons, well known from unpolarized reactions, knowledge of HOC's for Q, $\overline{Q}$ production in polarized processes is important for several special reasons.

Beginning with polarized $\gamma\gamma$ collisions, which is the subject of the present work, one reason of special interest is the following. A $\gamma\gamma$ collider becomes particularly important for searches of the standard model Higgs boson when its mass is below the W^+W^- threshold. Then the predominant decay is $H \to b\bar{b}$ and the background comes from $\gamma\gamma \to b\bar{b}$ with direct or resolved photons. Leaving aside the latter, for the moment, use of polarized photons of equal helicity (when the angular momentum has $J_z = 0$) suppresses this background by a factor m_b^2/s [4, 5]. This holds, however, only for the lowest order of α_s. HOC's necessarily involve the subprocess $\gamma\gamma \to b\bar{b}g$, and gluon emission permits the $b\bar{b}$ system to have $J \neq 0$ without suppression; this may result in a sizable background. Of course, another reason the $J_z = 0$ channel is important is that the Higgs boson signal comes entirely from it. Thus, we maximize the Higgs boson to background ratio in two different ways.

Furthermore, at higher energies, it will be possible to produce top quarks in photon-photon collisions. This, when combined with other data on top-quark production from e^+e^- and $p\bar{p}$ collisions, should certainly improve our knowledge of the top-quark parameters. The HOC's could have a significant effect on the threshold behavior. It is also interesting to examine the spin dependence of the HOC's in this region.

In this paper we present complete analytical results for heavy quark production by both polarized and unpolarized photons. Numerical results are presented for 2-, 3- and 2+3-jet cross sections for the cases where the initial photons have total spin $J_z = 0$ and $J_z = \pm 2$. For b-quark production, this is analyzed as a background to Higgs boson production. We also consider t-quark production for energies not too far above threshold.

The analytical results presented here are also useful in determining the production of heavy quarks in polarized photon-proton (proton-proton) collisions. This is because the process $\gamma\gamma \to Q\overline{Q}(g)$ is the Abelian (QED) part of the subprocess $\gamma g \to Q\overline{Q}(g)$ [$gg \to Q\overline{Q}(g)$], which is by far the dominant subprocess in γ-p (p-p) collisions [1, 2]. The non-Abelian part of $\vec{\gamma}\vec{g} \to Q\overline{Q}(g)$ [$\vec{g}\vec{g} \to Q\overline{Q}(g)$] remains to be calculated.

II. LEADING ORDER CROSS SECTIONS

The contributing graphs are shown in Fig. 1. We introduce the variables (momenta as in figure)

$$s \equiv (p_1 + p_2)^2, \quad t \equiv T - m^2 \equiv (p_1 - p_3)^2 - m^2,$$
$$u \equiv U - m^2 \equiv (p_2 - p_3)^2 - m^2 \tag{1}$$

and

$$s_2 \equiv S_2 - m^2 \equiv (p_1 + p_2 - p_3)^2 - m^2 = s + t + u, \tag{2}$$

where m is the heavy-quark mass. Defining

$$v \equiv 1 + \frac{t}{s}, \quad w \equiv \frac{-u}{s+t} \tag{3}$$

we may express

$$t = -s(1-v), \quad u = -svw, \quad s_2 = sv(1-w). \tag{4}$$

---

*On leave from High Energy Physics Institute, Tbilisi State University, Tbilisi, Republic of Georgia.

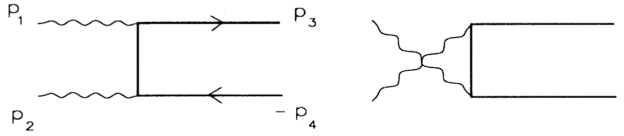

FIG. 1. Lowest order contributions to $\gamma\gamma \to Q\overline{Q}$.

The polarized and unpolarized squared amplitudes are defined, respectively, as

$$\begin{aligned}\Delta|M|^2 &\equiv \frac{1}{2}[|M(+,+)|^2 - |M(+,-)|^2],\\ |M|^2 &\equiv \frac{1}{2}[|M(+,+)|^2 + |M(+,-)|^2],\end{aligned} \tag{5}$$

where $M(\lambda_1,\lambda_2)$ denotes the Feynman amplitude with photons p_1, p_2 having helicity λ_1, λ_2 respectively. The same holds for the cross sections.

For the examples considered in this paper, it is of interest to calculate (numerically) the cross sections for a specific helicity state $\sigma(\lambda_1,\lambda_2)$. We present analytical results for the polarized and unpolarized cross sections $\Delta\sigma$, σ. From (5) we can obtain the desired cross sections via

$$\sigma(+,+) = \sigma + \Delta\sigma, \qquad \sigma(+,-) = \sigma - \Delta\sigma. \tag{6}$$

Defining

$$K(\varepsilon) \equiv \frac{m^{-2\varepsilon}}{s}\frac{\pi(4\pi)^{-2+\varepsilon}}{\Gamma(1-\varepsilon)}\left(\frac{tu - sm^2}{sm^2}\right)^{-\varepsilon} \tag{7}$$

we may express the n $(= 4 - 2\varepsilon)$-dimensional two-body phase space as

$$[\Delta]\frac{d\sigma_{2\to2}}{dvdw} = K(\varepsilon)\left[(2m)^2[\Delta]|M|^2_{2\to2}\right]\delta(1-w). \tag{8}$$

It will become necessary to work in n dimensions when we determine the HOC's (see next section for details).

The resulting leading-order (LO) cross sections are, in n dimensions,

$$\begin{aligned}\Delta\frac{d\sigma_{\rm LO}}{dvdw} &= 32\pi^2K(\varepsilon)\delta(1-w)N_C\alpha^2e_Q^4\mu^{4\varepsilon}\left\{-\frac{t^2+u^2}{tu} + 2\frac{sm^2}{tu}\left(\frac{s^2}{tu} - 2\right)\right\},\\ \frac{d\sigma_{\rm LO}}{dvdw} &= 32\pi^2K(\varepsilon)\delta(1-w)N_C\alpha^2e_Q^4\mu^{4\varepsilon}\left\{\frac{t^2+u^2}{tu} + 4\frac{sm^2}{tu} - 4\left(\frac{sm^2}{tu}\right)^2\right\},\end{aligned} \tag{9}$$

where N_C (=3) is the number of quark colors and e_Q is the fractional charge of the heavy quark. Making use of (4) and (6) we see explicitly that $d\sigma_{\rm LO}(+,+)/dvdw$ is suppressed by order m^2/s.

III. LOOP CONTRIBUTIONS

The loop contributions arise from the diagrams of Fig. 2 and their $p_1 \leftrightarrow p_2$ interchange. These diagrams contain both ultraviolet and infrared singularities. To regularize them, we use dimensional reduction [6], where the momenta are in n dimensions and everything else is in four dimensions. This facilitates the handling of the Levi-Civita tensor $\varepsilon^{\mu\nu\lambda\rho}$. As we will show below, the analytical expressions for the cross sections are *regularization scheme independent* once all the contributions (including the gluonic bremsstrahlung) are added. Throughout, we work in the Feynman gauge.

The heavy-quark mass and wave function renormalizations are performed on shell. The self energy graphs are shown in Figs. 2(a–c) and the corresponding mass counterterm diagrams in Figs. 2(a′–c′). The factor 1/2 multiplying (b)–(c′) comes from wave function renormalization. The bare mass and wave function are determined in terms of the renormalized ones via

$$m_0 = Z_m m_r, \qquad \Psi_0 = Z_2^{1/2}\Psi_r, \tag{10}$$

where Z_m and Z_2 are the mass and wave function renormalization constants. Define

$$C_\varepsilon \equiv \frac{\Gamma(1+\varepsilon)}{(4\pi)^2}\left(\frac{4\pi\mu^2}{m^2}\right)^{\varepsilon}, \tag{11}$$

where μ is an arbitrary mass scale which enters via the coupling in n dimensions: $g \to g\mu^\varepsilon$. In dimensional reduction we find, to order g^2,

$$\begin{aligned}Z_m &= 1 - 3g^2C_\varepsilon C_F\left(\frac{1}{\varepsilon'} + \frac{5}{3}\right),\\ Z_2 &= 1 - g^2C_\varepsilon C_F\left(\frac{1}{\varepsilon'} + 5 + \frac{2}{\varepsilon}\right)\end{aligned} \tag{12}$$

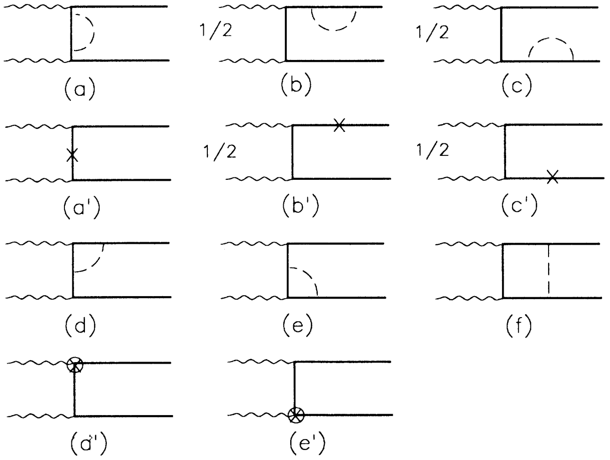

FIG. 2. Loop graphs for $\gamma\gamma \to Q\overline{Q}$. (a)–(c) self-energy diagrams; (a′)–(c′) mass counterterm diagrams corresponding to the graphs (a)–(c); (d),(e) vertex diagrams; (d′),(e′) dimensional reduction counterterm diagrams corresponding to graphs (d),(e); (f) box diagram.

with $C_F = 4/3$. We use $1/\varepsilon'$ to indicate which terms are of ultraviolet origin.

In dimensional reduction we must add to the vertex diagrams of Figs. 2(d,e) appropriate counterterms (d′, e′) in order to satisfy the Ward identity [7]

$$Z_1 = Z_2 \tag{13}$$

between vertex and self-energy graphs, with Z_1 denoting the vertex renormalization constant. The Feynman rule for this vertex counterterm is found to be (in n dimensions)

$$\gamma^\mu \to \frac{-g^2}{(4\pi)^2} C_F \gamma_\varepsilon^\mu \frac{1}{\varepsilon'} \tag{14}$$

with

$$\gamma_\varepsilon^\mu = (g^{\mu\nu} - g_n^{\mu\nu})\gamma_\nu, \qquad g_n^{\mu\nu} g_{\mu\nu}^n = g_n^{\mu\nu} g_{\mu\nu} = n; \tag{15}$$

here $g_n^{\mu\nu}$ represents the n-dimensional metric tensor with, formally, $n < 4$.

When all the contributions to the physical cross section (including gluonic bremsstrahlung) are added, the result is free of infrared divergences as there are no collinear singularities here. Thus the only scheme-dependent part might come from the vertex and self-energy graphs. Having satisfied the Ward identity (13), though, means that the scheme-dependent part of the corrections cancels between vertex and self-energy graphs. This was explicitly verified by calculating the vertex and self-energy graphs in dimensional regularization. We also checked explicitly that there are no differences between reduction and regularization arising from any other contributions. More specifically, to obtain the dimensional regularization result for any particular contribution given in this paper, simply replace the LO term by the corresponding LO term from dimensional regularization. When all the contributions are added, the scheme-dependent part of the LO term cancels along with the $1/\varepsilon$ infrared divergence multiplying it. Hence, the absence of collinear divergences or vacuum polarization graphs leads to scheme-independence.

As was stated in Refs. [8] and [9], a counterterm like (14) was used to remove an unphysical term. General one-loop counterterms have been developed [10] to convert unpolarized dimensional reduction results into the corresponding dimensional regularization results for the purely massless case. Also, certain equivalences between dimensional reduction and dimensional regularization have been noted [11]. In the present case, however, satisfaction of (13) is sufficient to ensure scheme-independence.

Adding the contributions of Figs. 2(a–e′) (and the $t \leftrightarrow u$ interchange) resulted in the ultraviolet finite vertex plus self-energy cross section

$$\frac{d\sigma_{\mathrm{VSE}}}{dv\,dw} = -\frac{16}{\varepsilon}\pi\alpha_s C_F C_\varepsilon \frac{d\sigma_{\mathrm{LO}}}{dv\,dw} + \delta(1-w)\frac{CK(0)}{(4\pi)^2}\Bigg(2A_1\Bigg\{4\left[\xi(2) - \mathrm{Li}_2\left(\frac{T}{m^2}\right)\right]\left(1+3\frac{m^2}{t}\right)$$
$$-\ln\left(-\frac{t}{m^2}\right)\left(8-6\frac{t}{T}-\frac{t^2}{T^2}\right) - 2 - \frac{t}{T}\Bigg\} + A_2\ln\left(-\frac{t}{m^2}\right) + A_3\left[\mathrm{Li}_2\left(\frac{T}{m^2}\right) - \xi(2)\right] + A_4 + (t \leftrightarrow u)\Bigg) \tag{16}$$

where

$$C \equiv (4\pi)^3 C_F N_C \alpha_s \alpha^2 e_Q^4 \mu^{6\varepsilon}. \tag{17}$$

The corresponding polarized cross section $\Delta d\sigma_{\mathrm{VSE}}/dv\,dw$ can be obtained by replacing the A_i and $d\sigma_{\mathrm{LO}}/dv\,dw$ in (16) by ΔA_i and $\Delta d\sigma_{\mathrm{LO}}/dv\,dw$, respectively.

The $[\Delta]A_i$ are given in Appendix B. We will use this notation throughout. We note the term $\sim 1/\varepsilon$ in (16) representing an infrared divergence. Also, note that $[\Delta]A_1$ is proportional to the LO squared amplitude without the $t \leftrightarrow u$ interchange [see Appendix B, Eq. (B3)].

Since $[\Delta]d\sigma_{\mathrm{LO}}/dv\,dw$ is in general regularization scheme dependent to $O(\varepsilon)$ (working in n dimensions), we see explicitly that truly scheme-independent cross sections will result only when all contributions are added and all infrared divergences are cancelled.

In order to evaluate the box graph of Fig. 2(f), we must reduce the resulting tensor integrals to scalar ones (conveniently listed in Ref. [2]) using projective tensor techniques [12]. The tensor integrals have the general form

$$D^{0,\mu,\mu\nu,\mu\nu\lambda}(k_1,k_2,k_3,m_1,m_2,m_3,m_4)$$
$$\equiv \mu^{2\varepsilon}\int\frac{d^n q}{(2\pi)^n}\frac{1,\,q^\mu,\,q^\mu q^\nu,\,q^\mu q^\nu q^\lambda}{(q-m_1)^2[(q+k_1)^2-m_2^2][(q+k_1+k_2)^2-m_3^2][(q+k_1+k_2+k_3)^2-m_4^2]}\,, \tag{18}$$

where the k_i are general momenta. As an example, the vector box integral we encounter has the decomposition

$$D^\mu(p_4,-p_2,-p_1,0,m,m,m) = p_4^\mu D_{11} - p_2^\mu D_{12} - p_1^\mu D_{13}. \tag{19}$$

In general, the scalar coefficients D_{ij} are not independent. This simplifies somewhat the calculation. Noting that

$$D^{\mu}(p_4,-p_2,-p_1,0,m,m,m) = -D^{\mu}(p_3,-p_1,-p_2,0,m,m,m), \tag{20}$$

we obtain

$$D_{12} = D_{11} - D_{13}, \tag{21}$$

since the D_{ij} in both integrals are the same, due to the fact that they are scalars. Using the same approach, we reduce the number of independent D_{ij} from seven to five in $D^{\mu\nu}$ and from thirteen to eight in $D^{\mu\nu\lambda}$. This method was quite helpful in keeping the very large intermediate expressions as short as possible.

Adding the contribution of Fig. 2(f) and the $t \leftrightarrow u$ interchange gives the virtual box cross section

$$\begin{aligned}\frac{d\sigma_{\rm box}}{dvdw} &= 16\pi\alpha_s C_F C_\varepsilon \frac{d\sigma_{\rm LO}}{dvdw}\frac{2m^2-s}{s\beta}\left\{2\ln(x)\left[\frac{1}{2\varepsilon}-\ln(\beta)\right]+2{\rm Li}_2(-x)-2{\rm Li}_2(x)-3\xi(2)\right\}\\ &\quad+\delta(1-w)\frac{CK(0)}{(4\pi)^2}\left\{-8B_1\frac{2m^2-s}{s\beta}\ln(x)\ln(-t/m^2)+2\frac{B_2}{\beta}\{\ln(x)[4\ln(1+x)-\ln(x)\right.\\ &\quad-4\ln(-t/m^2)]+4{\rm Li}_2(-x)+2\xi(2)\}+2B_3\ln^2(x)+4\frac{B_4}{\beta}\ln(x)+4B_5\ln(-t/m^2)\\ &\quad\left.+8B_6{\rm Li}_2(T/m^2)+4B_7\xi(2)+4B_8+(t\leftrightarrow u)\right\},\end{aligned} \tag{22}$$

where

$$\xi(2) = \frac{\pi^2}{6}, \qquad \beta \equiv \sqrt{1-4m^2/s}, \qquad x \equiv \frac{1-\beta}{1+\beta}. \tag{23}$$

The $[\Delta]B_i$ are given in Appendix B. We see again the infrared divergence $\sim 1/\varepsilon$.

Independent calculations were performed using FORM [13] and REDUCE [14]. The latter proved useful in factoring the expressions and cancelling powers in the denominators.

IV. GLUONIC BREMSSTRAHLUNG CONTRIBUTIONS

The bremsstrahlung diagrams are shown in Fig. 3. Squaring these diagrams (plus their $p_1 \leftrightarrow p_2$ interchange), we obtain the $2 \to 3$ particle squared amplitude

$$\begin{aligned}(2m)^2|M|^2_{2\to3} = C&\left[\frac{\tilde{e}_1}{s_2^2}+e_2\,p_2\cdot k+\frac{e_3}{p_2\cdot p_4}+\frac{e_4}{p_2\cdot p_4^2}+e_5\frac{p_2\cdot k}{p_1\cdot p_4^2}+\frac{\tilde{e}_6}{s_2\,p_3\cdot k}+\frac{\tilde{e}_7}{p_3\cdot k^{\,2}}+\frac{e_8}{p_1\cdot p_4\,p_2\cdot p_4}\right.\\ &+e_9\frac{p_2\cdot k^{\,2}}{p_1\cdot p_4}+e_{10}\frac{p_2\cdot k}{p_1\cdot p_4}+\frac{\tilde{e}_{11}/s_2}{p_2\cdot p_4\,p_3\cdot k}+\frac{\tilde{e}_{12}}{p_2\cdot p_4\,p_3\cdot k^{\,2}}+\frac{e_{13}}{p_2\cdot p_4^2\,p_3\cdot k}\\ &\left.+\frac{\tilde{e}_{14}}{p_2\cdot p_4^2\,p_3\cdot k^{\,2}}+e_{15}\frac{p_2\cdot k^{\,2}}{p_3\cdot k}+e_{16}\frac{p_2\cdot k}{p_3\cdot k}\right]+(p_1\leftrightarrow p_2, t\leftrightarrow u)\ .\end{aligned} \tag{24}$$

As before, we may obtain $\Delta|M|^2_{2\to3}$ by replacing the e_i in (24) by Δe_i. The $[\Delta]e_i$ are given in Appendix B. Again, independent calculations were performed using FORM and REDUCE. The former proved useful in partial fractioning and other reductions of the dot products.

To obtain the total bremsstrahlung contribution to $[\Delta]d\sigma/dvdw$, we perform the phase-space integrations in the frame where p_4 and k are back to back. We find (in agreement with Ref. [2]), for the $2 \to 3$ phase space,

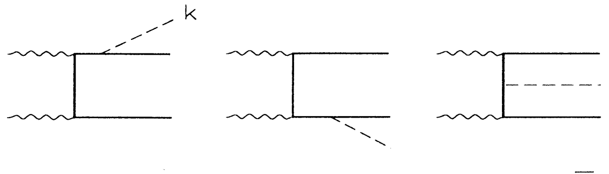

FIG. 3. Gluonic bremsstrahlung graphs for $\gamma\gamma \to Q\overline{Q}g$.

$$[\Delta]\frac{d\sigma_{\rm Br}}{dvdw} = K(\varepsilon)\frac{C_\varepsilon}{\mu^{2\varepsilon}}\tilde{f}(\varepsilon)\int d\Omega(2m)^2[\Delta]|M|^2_{2\to3}\ , \tag{25}$$

where

$$\tilde{f}(\varepsilon) \equiv \frac{(m^2)^{1-\varepsilon}}{S_2^{1-\varepsilon}}\frac{sv}{2\pi}\left(\frac{sv}{m^2}\right)^{1-2\varepsilon}(1-w)^{1-2\varepsilon} \tag{26}$$

and

$$\int d\Omega \equiv \int_0^{\pi} d\theta_1 \sin^{1-2\varepsilon}\theta_1 \int_0^{\pi} d\theta_2 \sin^{-2\varepsilon}\theta_2. \tag{27}$$

The gluon angles θ_1 and θ_2 are defined in Appendix A along with all the momenta.

We first evaluate all the phase space integrals in four dimensions since, for $w \neq 1$, all the integrals are finite. For $w = 1$, the terms in (24) with coefficients $\tilde{e}_i$ are singular through the relation [15]

$$(1-w)^{-1-2\varepsilon} = -\frac{1}{2\varepsilon}\delta(1-w) + \frac{1}{(1-w)_+} + O(\varepsilon)\ , \tag{28}$$

where the function $1/(1-w)_+$ is defined through

$$\int_{w_1}^{1} dw \frac{f(w)}{(1-w)_+} = \int_{w_1}^{1} dw \frac{f(w)-f(1)}{(1-w)} + f(1)\ln(1-w_1). \tag{29}$$

This means that, for these terms, the integrals must also be evaluated in n dimensions in the limit $w \to 1$, keeping their $O(\varepsilon)$ part. The resulting integrals are straightforward.

The final result is, with $\bar{y} \equiv \sqrt{(t+u)^2 - 4m^2 s}$,

$$\begin{aligned}\frac{d\sigma_{\rm Br}}{dvdw} = {} & \frac{CK(0)}{(4\pi)^2} 2\pi \tilde{f}(0) \left\{ \frac{s_2(s+u)}{4S_2} e_2 + \frac{2S_2}{s_2(s+u)} \ln\frac{S_2}{m^2}\ e_3 + \frac{4S_2}{m^2(s+u)^2} e_4 + e_5 I_5 + e_8 I_8 + e_9 I_9 + e_{10} I_{10} + e_{13} I_{13} \right. \\ & \left. + e_{15} I_{15} + e_{16} I_{16} + (t \leftrightarrow u) \right\} \\ & + \frac{1}{(1-w)_+} \frac{CK(0)}{(4\pi)^2} \frac{1}{S_2} \left\{ \tilde{e}_1 + \frac{2S_2}{\bar{y}} \ln\frac{T+U-\bar{y}}{T+U+\bar{y}}\ \tilde{e}_6 + 4\frac{S_2}{m^2}\tilde{e}_7 + s_2 I_{11}\tilde{e}_{11} + s_2^2 I_{12}\tilde{e}_{12} + s_2^2 I_{14}\tilde{e}_{14} + (t \leftrightarrow u) \right\} \\ & + 8\pi\alpha_s C_F C_\varepsilon \frac{d\sigma_{\rm LO}}{dvdw} \frac{1}{s\beta} \left((2m^2 - s) \left\{ 2\ln x \left(2\ln\frac{sv}{m^2} - \frac{1}{\varepsilon} \right) - 1 - 2\left[{\rm Li}_2\left(\frac{-4\beta}{(1-\beta)^2} \right) + \ln^2 x \right] \right\} \right. \\ & \left. + 2s\beta \left[1 - 2\ln\frac{sv}{m^2} + \frac{1}{\varepsilon} \right] \right), \end{aligned} \tag{30}$$

where the integrals I_i are given in Appendix C.

V. PHYSICAL CROSS SECTIONS

We may obtain the 2+3-jet cross section by adding (9), (16), (22), and (30):

$$[\Delta]\frac{d\sigma_{2+3}}{dvdw} = [\Delta]\frac{d\sigma_{\rm LO}}{dvdw} + [\Delta]\frac{d\sigma_{\rm VSE}}{dvdw} + [\Delta]\frac{d\sigma_{\rm box}}{dvdw} + [\Delta]\frac{d\sigma_{\rm Br}}{dvdw}\ . \tag{31}$$

We notice the cancellation of all the $1/\varepsilon$ infrared divergences, leading to a finite, scheme-independent result.

At this point it is useful to note that for $s \gg 4m^2$, the LO cross sections (9) are large in the forward and backward directions. Since jets going down the beam pipe are difficult to measure experimentally, angular cuts are necessary for $b\bar{b}$ production well above threshold. At the same time, we reduce the $b\bar{b}$ background to the Higgs signal. This also helps eliminate *resolved photon* contributions where the partons within the photon participate, as opposed to the *direct* contributions, which we present, where the photon is structureless. This is discussed at the end of this section.

Let θ_3 denote the angle between p_3 and p_1 in the $\gamma\gamma$ c.m. Then the integrated 2+3-jet cross section, with the constraint $|\cos\theta_3| < \cos\theta_C$, for some θ_C, is given by

$$[\Delta]\sigma_{2+3}(s) = \int_{v_1}^{v_2} dv \int_{w_1}^{1} dw\ \Theta(\cos^2\theta_C - \cos^2\theta_3)[\Delta]\frac{d\sigma_{2+3}}{dvdw}\ , \tag{32}$$

where

$$v_1 = \frac{1}{2}(1-\beta), \qquad v_2 = \frac{1}{2}(1+\beta), \qquad w_1(v) = \frac{m^2}{s}\frac{1}{v(1-v)} \tag{33}$$

and

$$\cos\theta_3 = \frac{-(1-v-vw)}{\sqrt{(1-v+vw)^2 - 4m^2/s}}. \tag{34}$$

Alternatively, we may convert to $d\sigma/d\cos\theta_3 dw$ and integrate directly over θ_3 and w.

The integrated 3-jet cross section is given by

$$\begin{aligned}[\Delta]\sigma_3(s) = {} & \frac{K(0)}{(4\pi)^2} \int_{v_1}^{v_2} dv \int_{w_1}^{1} dw\ \Theta(\cos^2\theta_C - \cos^2\theta_3)\tilde{f}(0) \int d\Omega (2m)^2 [\Delta] |M|^2_{2\to3} \\ & \times\Theta((p_3+k)^2 - y_{\rm cut}s)\Theta((p_4+k)^2 - y_{\rm cut}s) \\ = {} & \frac{K(0)}{(4\pi)^2} \int_{v_1}^{v_2} dv \int_{w_1}^{w_2} dw\ \Theta(\cos^2\theta_C - \cos^2\theta_3)\tilde{f}(0) \int d\Omega (2m)^2 [\Delta] |M|^2_{2\to3} \\ & \times\Theta((p_3+k)^2 - y_{\rm cut}s), \qquad w_2 = 1 - \frac{y_{\rm cut} - m^2/s}{v}. \end{aligned} \tag{35}$$

The angular integral is given by (27) with $\varepsilon = 0$. The dot products involved may be explicitly expressed as functions of v, w, θ_1, and θ_2 using the parametrizations of Appendix A and Eqs. (4). We have imposed the constraints $(p_3 + k)^2 > y_{\rm cut}s$ and $(p_4 + k)^2 > y_{\rm cut}s$. With a suitable choice of $y_{\rm cut}$ we may simultaneously cut out events with 2-jet topology and avoid the soft divergence. We effectively eliminate the soft and collinear gluons from the 3-jet cross section, with the degree of softness and collinearity being specified by $y_{\rm cut}s$.

The desired 2-jet cross section is obtained by the difference

$$[\Delta]\sigma_2(s) = [\Delta]\sigma_{2+3}(s) - [\Delta]\sigma_3(s). \tag{36}$$

Since σ_{2+3} and σ_3 are both infrared finite and separately observable quantities, this serves as a reliable and unambiguous method for defining σ_2.

In discussing the numerical results, it will be convenient to split $[\Delta]\sigma_{2+3}$ as

$$[\Delta]\sigma_{2+3} = [\Delta]\sigma_{\rm LO} + [\Delta]\sigma_{\rm S} + [\Delta]\sigma_H, \tag{37}$$

where $[\Delta]\sigma_{\rm S}$ represents the contribution to the HOC's coming from terms proportional to $\delta(1-w)$ and $1/(1-w)_+$, and $[\Delta]\sigma_H$ represents the rest. In usual terminology, $[\Delta]\sigma_{\rm S}$ represents virtual and soft contributions whereas $[\Delta]\sigma_H$ represents hard radiation.

So far we have only considered direct contributions, i.e., no resolved photon contributions. The reason is the following. Well above the $Q\overline{Q}$ threshold, σ_{2+3} and σ_3 will certainly receive sizable resolved photon contributions. Now, resolved photon events are generally accompanied by a jet making small angles with respect to the beam axis. For the 2-jet cross section (which is of physical interest), experiment can reject resolved photon events (and other unwanted events) as being those for which the observed jets have total energy measurably lower than $\sqrt{s}$ [5]. This is because, due to the angular cuts, experiment will not observe the jet making small angles. Hence, there will be missing energy. Of course, we are assuming a rather well-defined initial photon energy, which may be experimentally difficult.

For top-quark production, not too far above threshold, the resolved contributions will be negligible in all the cross sections. This is because the dominant resolved contribution comes from $g\gamma \to Q\overline{Q}$, where the gluon originates from one of the initial photons, having a fraction x of its momentum. Near threshold, the gluon will have to carry a large fraction of the photon's momentum; and for $x \to 1$, the gluon distribution in the photon is highly suppressed. As well, 3-jet states arising from hard gluonic radiation will be suppressed due to the restricted phase space. The (near) absence of resolved contributions and the nonsuppression of the $J_z = 0$ cross section for $2 \to 2$ kinematics, not too far above threshold, implies that we need not worry about whether the events are 2- or 3-jet (even though 3-jet events are either very seldom or none, depending on s).

VI. NUMERICAL RESULTS

Here we present numerical results for b- and t-quark production in next-to-leading order. Throughout, we evaluate $\alpha_s(Q^2)$ (two-loop) with $Q^2 = s$, $\Lambda = 0.2$ GeV, and the number of flavors taken as $N_F = 5$ since we are well above the $b\bar{b}$ threshold. We take $m_b = 4.7$ GeV and $m_t = 174$ GeV [16]. For 3-jet cross sections, we use $y_{\rm cut} = 0.15$. Some justification for this choice of $y_{\rm cut}$ is in order. Experimentally, it is useful to have a small value of $y_{\rm cut}$ so that for the 2-jet cross section we eliminate, as much as possible, events with 3-jet topology via (36). Theoretically, there are limitations. If one chooses $y_{\rm cut}$ too small, then the infrared divergence ruins the perturbation expansion, since the 3-jet cross section becomes unphysically large. To control this, an all-orders resummation would be required. We find that $y_{\rm cut} = 0.15$ is the most suitable choice in light of the above considerations.

Figure 4(a) presents $\sigma_{\rm LO}(+,+)$, $\sigma_{2+3}(+,+)$, $\sigma_3(+,+)$, and $\sigma_2(+,+)$ for b-quark production in the range $20 < \sqrt{s} < 200$ GeV with $\theta_C = 30°$. As expected, the LO cross section is highly suppressed for large $\sqrt{s}$, but not the 3-jet. In fact $\sigma_3(+,+)$ makes a sizable contribution to $\sigma_{2+3}(+,+)$. Hence $\sigma_2(+,+)$ gets somewhat suppressed relative to $\sigma_{2+3}(+,+)$. For $20 \lesssim \sqrt{s} \lesssim 40$ GeV the corrections $\sigma_{2+3} - \sigma_{\rm LO}$ are seen to be slightly negative.

Figure 4(b) presents the same cross sections for $J_z = \pm 2$, i.e., $\sigma_{\rm LO}(+,-)$, $\sigma_{2+3}(+,-)$, $\sigma_3(+,-)$, and $\sigma_2(+,-)$. The major difference is that $\sigma_{\rm LO}(+,-)$ and $\sigma_{2+3}(+,-)$ suffer no suppression at large $\sqrt{s}$. Hence the 3-jet contribution to $\sigma_{2+3}(+,-)$ is not so significant and $\sigma_2(+,-)$

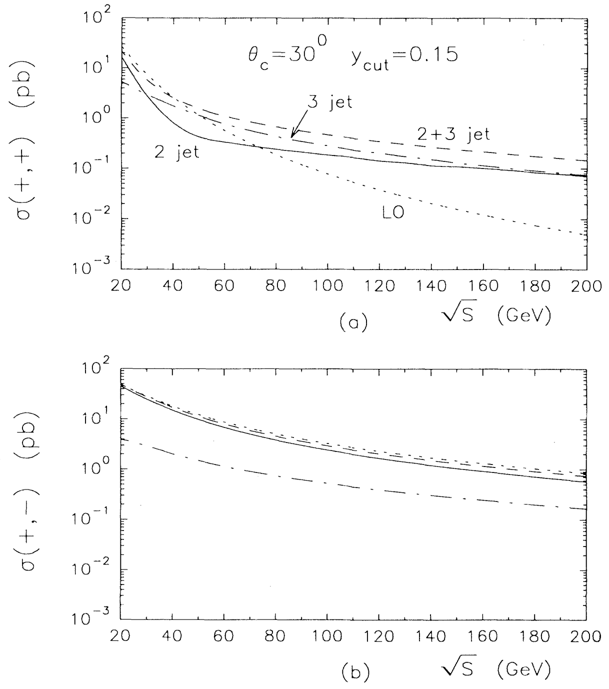

FIG. 4. Cross sections for $\gamma\gamma \to b\bar{b}(g)$: $\sigma_{\rm LO}$ (dotted line), σ_{2+3} (dashed), σ_3 (dash-dotted), and σ_2 (solid), with $\theta_C = 30°$ and $y_{\rm cut} = 0.15$ for $20 < \sqrt{s} < 200$ GeV; (a) $\sigma(+,+)$; (b) $\sigma(+,-)$.

remains large. We also notice $\sigma_{2+3} \lesssim \sigma_{\rm LO}$ throughout.

Figures 5(a,b) present the same quantities as in Figs. 4(a,b) except with $\theta_C = 45°$. The major difference is that the cross sections are smaller everywhere and $\sigma_2(+,+)$ is particularly suppressed for $30 \lesssim \sqrt{s} \lesssim 60$ GeV. This reflects the fact that the 2-jet events tend to occur at smaller angles.

An interesting feature of the HOC arises for both σ_{2+3} and $\Delta\sigma_{2+3}$. In both cases, σ_S and σ_H are much larger that $\sigma_{\rm LO}$, for $s \gg 4m^2$. But they have opposite sign and are of almost equal magnitude, leading to large cancellations. In other words, the "virtual + soft" part conspires with the "hard" part to yield HOC's which are under control.

Figure 6 presents the 2-jet background to the Higgs boson decay $\gamma\gamma \to H^* \to b\bar{b}$. We have used the standard model Higgs cross section of Ref. [4] which takes $\theta_C = 30°$ and an average value of $\langle\lambda_1\lambda_2\rangle = 0.8$. The photons are produced by laser backscattering off electrons (positrons) at an e^+e^- collider with $E_{e^+e^-} = 500$ GeV. As well, Ref. [4] uses an effective integrated luminosity of $L_{\rm eff} = 20{\rm fb}^{-1}$ and a $\gamma\gamma$ energy spread of $\Gamma_{\rm expt} = 5$ GeV; $\sqrt{s} = m_H \pm \Gamma_{\rm expt}/2$. Using the expression of Ref. [4] for converting the $\gamma\gamma \to b\bar{b}(g)$ cross section into a number of events, we obtain the LO and 2-jet curves shown in Fig. 6.

At large $\sqrt{s}$, the increase in $\sigma_2(+,+)$ relative to $\sigma_{\rm LO}(+,+)$ is compensated by a decrease in $\sigma_2(+,-)$ relative to $\sigma_{\rm LO}(+,-)$, so that $\sigma_2(\langle\lambda_1\lambda_2\rangle = 0.8)$ does not change radically. In the end, the 2-jet cross section is still well below the Higgs signal for $90 \lesssim m_H \lesssim 150$ GeV. With higher degrees of polarization, we could do even better.

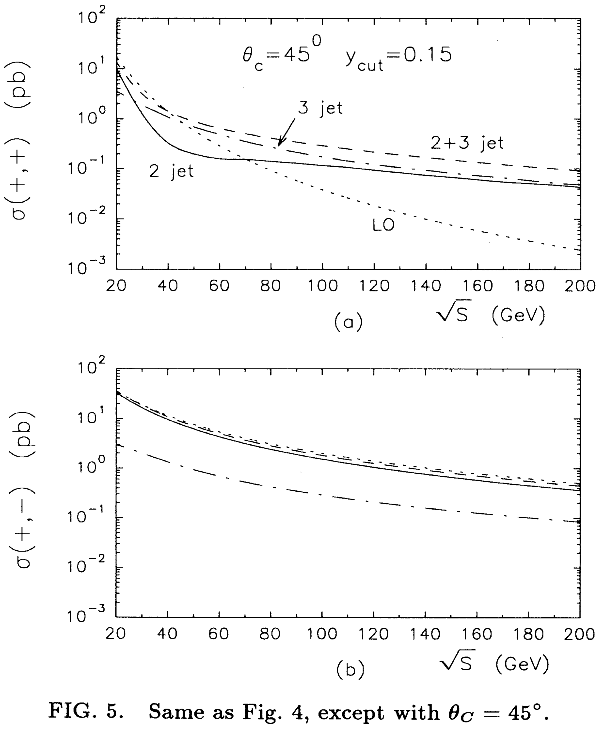

FIG. 5. Same as Fig. 4, except with $\theta_C = 45°$.

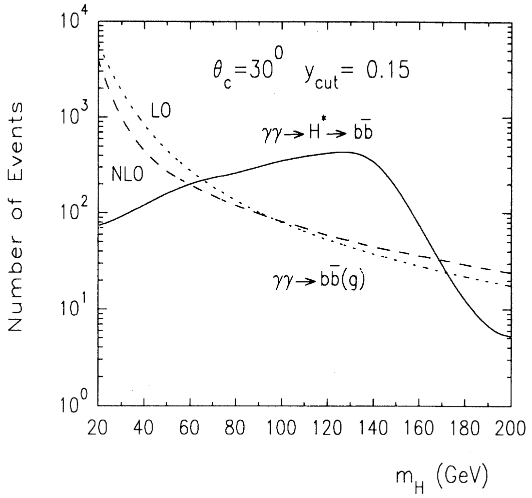

FIG. 6. Two-jet $b\bar{b}$ background to standard model Higgs boson decay: $\gamma\gamma \to H^* \to b\bar{b}$ (solid line), $\sigma_{\rm LO}$ (dotted), and σ_2 (dashed) for $20 < m_H < 200$ GeV. Number of Higgs events taken from Ref. [4]. Here $\theta_C = 30°$, $< \lambda_1\lambda_2 >= 0.8$. The other experimental parameters are described in the text.

Figure 7(a) gives σ_{2+3} and $\sigma_{\rm LO}$ for t-quark production in the range $1 < \sqrt{s}/2m < 1.4$ for $J_z = 0$ and $J_z = \pm 2$, without angular cuts. Figure 7(b) is the same except with $\theta_C = 30°$. We notice that the angular cuts do not make a big difference. This is because there is no peaked behavior in the forward or backward directions

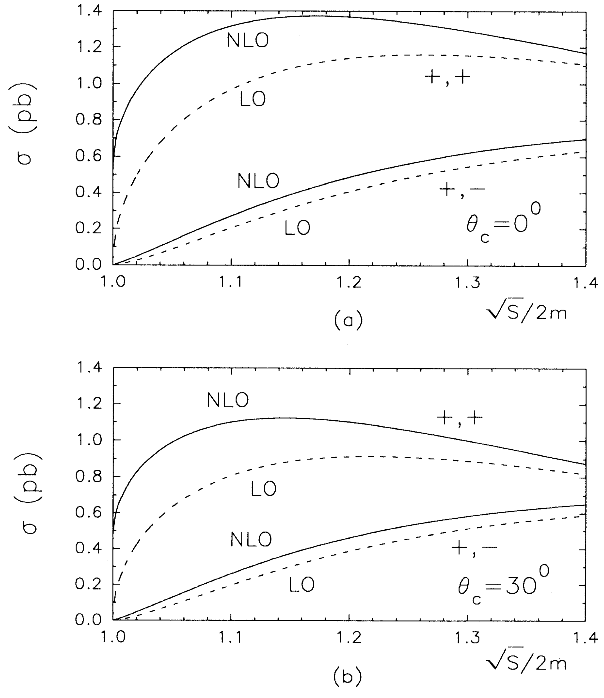

FIG. 7. Cross sections for $\gamma\gamma \to t\bar{t}(g)$: $\sigma_{\rm LO}(+,-)$ (lower dashed line), $\sigma_{2+3}(+,-)$ (lower solid), $\sigma_{\rm LO}(+,+)$ (upper dashed), and $\sigma_{2+3}(+,+)$ (upper solid) for $1 < \sqrt{s}/2m < 1.4$: (a) $\theta_C = 0$; (b) $\theta_C = 30°$.

as for $b\bar{b}$ production. As explained earlier, the (near) absence of resolved contributions makes the angular cuts less important experimentally as well. The most interesting feature of the HOC is that just above threshold, the HOC to $\sigma(+,+)$ completely dominate. There is no similar behavior from $\sigma(+,-)$. This suggests that the $J_z = 0$ channel is ideal for maximizing the top cross section not too far above threshold. At any rate, this drastic spin dependence of the HOC is of theoretical interest by itself and could be tested at the $b\bar{b}$ threshold as well. As the cross section is actually a function of only $\sqrt{s}/m$ (or β) and $\alpha_s(Q^2)$ (times an overall factor of e_Q^4/s), the only difference would be an increase in the HOC for $b\bar{b}$ relative to its corresponding LO term, due to an increase in α_s. In fact, the only ambiguity in the predictions is the choice of scale Q^2 in $\alpha_s(Q^2)$. Varying Q^2 in the range $s/4 < Q^2 < 4s$, for $\sqrt{s} = 400$ GeV, gives α_s in the range $0.0878 < \alpha_s < 0.104$ and a corresponding variation in the magnitude of the corrections.

Figure 8 gives the unpolarized cross sections corresponding to Fig. 7(a). We also plot the small β (threshold region) approximation of Ref. [3]. Our results agree with this approximation just above threshold. We see that the approximation breaks down for $\sqrt{s}/2m \gtrsim 1.02$. As expected, we found that almost all of the correction comes from σ_S, i.e., σ_H is almost negligible not too far above threshold. We found the same was true for $\Delta\sigma_S$, $\Delta\sigma_H$.

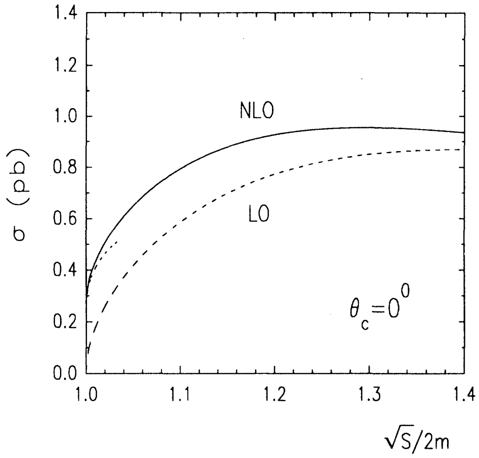

FIG. 8. Unpolarized cross sections corresponding to Fig. 7(a): σ_{2+3} (solid line), $\sigma_{\rm LO}$ (dashed), and the small β approximation (dotted).

VII. CONCLUSIONS

We have obtained complete analytical results for the production of heavy-quark pairs by polarized and unpolarized photons in next-to-leading order. Using these expressions, we computed cross sections for b- and t-quark production by photons having net spin $J_z = 0, \pm 2$. From the $b\bar{b}$ cross sections, we determined the background to $\gamma\gamma \to H^* \to b\bar{b}$ (standard model) coming from $\gamma\gamma \to b\bar{b}(g)$ (2-jet) for $\langle\lambda_1\lambda_2\rangle = 0.8$. The HOC's to the $J_z = 0$ channel were found to be large for $s \gg 4m^2$. For the experimental setup considered, the background was safely below the Higgs signal (but still sizable) for $90 \lesssim m_H \lesssim 150$ GeV, even after inclusion of HOC's. For t-quark production, not too far above threshold, the dominant contribution came from the $J_z = 0$ channel. Just above threshold, the HOC's to this channel completely dominate.

ACKNOWLEDGMENTS

We would like to thank D. Atwood, G. Jikia, and O. Teryaev for discussions and J. Peralta for help in the early stages. This work was also supported by the Natural Sciences and Engineering Research Council of Canada and by the Quebec Department of Education.

APPENDIX A

Here we present the momentum parametrizations in the frame where p_4 and k are back to back. We find

$$\begin{aligned}
p_1 &= (\omega_1; 0, \ldots, |\mathbf{p}|\sin\psi, |\mathbf{p}|\cos\psi - \omega_2),\\
p_2 &= (\omega_2; 0, \ldots, 0, \omega_2),\\
k &= (\omega_k; \ldots, \omega_k \sin\theta_1 \cos\theta_2, \omega_k \cos\theta_1),\\
p_4 &= (E_4; \ldots, -\omega_k \sin\theta_1 \cos\theta_2, -\omega_k \cos\theta_1),\\
p_3 &= (E_3; 0, \ldots, |\mathbf{p}|\sin\psi, |\mathbf{p}|\cos\psi),
\end{aligned} \tag{A1}$$

where

$$\begin{aligned}
&\omega_1 = \frac{s+t}{2\sqrt{S_2}}, \quad \omega_2 = \frac{s+u}{2\sqrt{S_2}}, \quad \omega_k = \frac{s_2}{2\sqrt{S_2}},\\
&E_4 = \frac{s_2 + 2m^2}{2\sqrt{S_2}}, \quad E_3 = -\frac{T+U}{2\sqrt{S_2}}, \quad |\mathbf{p}| = \frac{\bar{y}}{2\sqrt{S_2}},\\
&\cos\psi = \frac{us_2 - s(t+2m^2)}{(s+u)\bar{y}}\ ,
\end{aligned} \tag{A2}$$

in agreement with Ref. [2]. For p_1, p_2, p_3 the ellipses represent zeros. For k, p_4 they represent components which depend on the remaining $n-4$ angles of k. Since these components do not contribute to $[\Delta]|M|^2_{2\to 3}$, those angles were trivially integrated over in the phase space (25).

APPENDIX B

In this appendix we list the coefficients for the various cross sections. For $\Delta d\sigma_{\rm VSE}/dvdw$ given in Eq. (16), the coefficients ΔA_i are

$$\begin{aligned}
\Delta A_1 &= 2[-1 - u/s + u^2/st + m^2 s/tu - 2m^2 u/t^2],\\
\Delta A_2 &= -4[4(6u/t - 4s/u - t/T)m^2/t - 4sT/t^2 - 16s/t + 24u/s + s/T + 4tu/sT]m^2/T,\\
\Delta A_3 &= 16[(7s/t + 3 - 3t/u)m^4/t^2 + (4u^2/st + 2t/s - s^2/tu)m^2/t + t/s + u^2/st],\\
\Delta A_4 &= 4[4m^2 u/t^2 - 3s/t + 4u/s]m^2/T\ .
\end{aligned} \tag{B1}$$

For $d\sigma_{\rm VSE}/dvdw$ given in Eq. (16), the coefficients A_i are

$$\begin{aligned}
&A_1 = 2[u/t - 2m^2/t + sm^2/tu - 4m^4/tu - 4m^4/t^2],\\
&A_2 = 4[4(12sT/t^2 + t/T + 6)m^4/uT + (s^2/uT - 4s^2/tu - 4s^2T/t^2u - 12s/t - 2t/T - 8)m^2/T - 4],\\
&A_3 = 16[12m^6s/t^3u + (s/t - 14 - 8t/u)m^4/t^2 - (3s/t + 7 + t/u)m^2/t + u/t],\\
&A_4 = -4[4(2s/t + t/T)m^4/tu + (t/T - 4)m^2s^2/t^2u + 2t/T - 4] \; . \qquad \text{(B2)}
\end{aligned}$$

We note that

$$[\Delta]A_1 + (t \leftrightarrow u) = (2m)^2[\Delta]|M|^2_{\rm LO}/(N_C e^4 e_Q^4 \mu^{4\varepsilon}). \qquad \text{(B3)}$$

For $\Delta d\sigma_{\rm box}/dvdw$ given in Eq. (22), the coefficients ΔB_i are

$$\begin{aligned}
&\Delta B_1 = \Delta A_1,\\
&\Delta B_2 = 4(s + 4t)m^4/stu + 2(s/u + 4u/s)m^2/s - s^2/tu - 2s/u + t/u - 4u/s,\\
&\Delta B_3 = 12m^4/tu + 2m^2(t - u)/tu - s^2/tu - t/u \; ,\\
&\Delta B_4 = [8(t - u)/s - 3s/t - s/u]m^2/s + 5u/s - t/s \; ,\\
&\Delta B_5 = 4sT/tu + (t/u - 1)m^2t^2/sT^2 + 4(s^2 - 2t^2)/st - 7tu/sT + t^2(s - 3t)/sTu \; ,\\
&\Delta B_6 = 2(s/t - 4)m^4/tu - 2m^2(t - u)/tu + s^2/tu + t/u \; ,\\
&\Delta B_7 = 4(u - 4t)m^4/t^2u + 2m^2(u - t)/tu + s^2/tu + t/u; \quad \Delta B_8 = (1 + t^2/Ts)(t/u - 1) \; . \qquad \text{(B4)}
\end{aligned}$$

For $d\sigma_{\rm box}/dvdw$ given in Eq. (22), the coefficients B_i are

$$\begin{aligned}
&B_1 = A_1; \quad B_2 = (2m^2 - s)[(2m^2 - u)/st - 2/u] - 2m^2(6m^2 + t)/su \; ,\\
&B_3 = -4m^4/tu + 2m^2(u - t)/tu + s^2/tu + t/u; \quad B_4 = -2m^2s/tu + 2 \; ,\\
&B_5 = 2[(2m^2 + s)(2s/t + t/T) - t^3/T^2]/u; \quad B_6 = 8m^4/tu + 2m^2/u - s^2/tu - t/u \; ,\\
&B_7 = -4m^4/tu + 2m^2(t - 3u)/tu - s^2/tu - t/u; \quad B_8 = 2(s + t^2/T)/u \; . \qquad \text{(B5)}
\end{aligned}$$

For $\Delta|M|^2_{2\to 3}$ given in Eq. (24) and $\Delta d\sigma_{\rm Br}/dvdw$ given in Eq. (30), the coefficients Δe_i are

$$\begin{aligned}
\Delta\tilde{e}_1 = {}& -16(s/u - s/t - 2)m^4/u - 4[s_2(2 + 2s/u - t/s + u/s + 2t^2/s^2 + 8tu/s^2) + 2s - 4tu/s]m^2/u\\
&+ s_2(4s/u - 4 - 8t^2/su - 5t/s) \; ,
\end{aligned}$$

$$\Delta e_2 = -4[2m^2(2/s_2u + 2/s_2t + 1/s^2 - u/s^2t) + 6/t - t/s^2 + u^2/s^2t]/u \; ,$$

$$\begin{aligned}
\Delta e_3 = {}& -2[8m^4(1/tu - 1/s_2u - s/s_2t^2) - 2(4s/s_2 + s/t - 1)m^2/t - 3s/u - 5s/t\\
&-(2s^3/tu - su/t + 3t + 2u + u^2/t)/s_2] \; ,
\end{aligned}$$

$$\Delta e_4 = -2(2m^2s/t + 2s + u)m^2/t; \qquad \Delta e_5 = 0 \; ,$$

$$\Delta\tilde{e}_6 = [32m^4/u - 4m^2(t/u + 5 + t^2/su + 5t/s + 2t^3/s^2u + 10t^2/s^2 + 8tu/s^2) + 4st/u - 16t - 8t^2s_2/su - 5ts_2/s]/2;$$

$$\Delta\tilde{e}_7 = -2m^2 \; ,$$

$$\Delta e_8 = 4m^4(s/tu + 2/u + 1/s) - 2m^2(s^2/tu + 2s_2/u - 1 + t/s) - (s^2/t + s + 3s_2 + t^2/s + 3tu/s)s/u;$$

$$\Delta e_9 = 8(1/u - 1/s_2)/t \; ,$$

$$\Delta e_{10} = 4[2(1/u + 2s/s_2t - 2/s_2)m^2/u + s_2/tu - 3/s_2 - u/ts_2] \; ,$$

$$\begin{aligned}
\Delta\tilde{e}_{11} = {}& 8m^4(s/t + t/u + s_2/s) - 2m^2[2s^2/u + 2s^2/t + s + s_2(2t/u + 2 + 4u/t + t/s + u/s)]\\
&-(s^2 + t^2)(t + u)/u; \qquad \Delta\tilde{e}_{12} = m^2s; \qquad \Delta e_{13} = -m^2(4m^2s/t + 2s + u) \; ,
\end{aligned}$$

$$\Delta\tilde{e}_{14} = -m^4s; \qquad \Delta e_{15} = 4[2m^2/u - 2m^2/t - t/u + u/t]/s^2 \; ,$$

$$\Delta e_{16} = a_1 + a_1(t \leftrightarrow u) - 8(m^2 + m^2t/s - t)/su + 2[t^2(t/u + 2) - u^2(u/t + 2)]/s^2s_2 \; , \qquad \text{(B6)}$$

where

$$a_1 = t[4m^2(7s/t + 1 + 3t/s + 9u/s) - 2s + 6su/t + 4t + u]/s_2us \ . \tag{B7}$$

For $|M|^2_{2\to3}$ given in Eq. (24) and $d\sigma_{\rm Br}/dvdw$ given in Eq. (30), the coefficients e_i are

$$\begin{aligned}
\tilde e_1 &= 2[16m^6(t+u)/tu + 16m^4(s_2/u + s/t + 3) + 2m^2(25s_2 - 2t + 2s_2^2/u) \\
&\quad + s_2(2s + 5t + 10u)]/u; \qquad e_2 = -8[2m^2(t+u)/s_2t + 3]/tu \ , \\
e_3 &= -2[16m^6(t+u)/s_2tu + 8(4 + u/t - 2s/s_2)m^4/u + 2m^2(6t/u + 6 - u/t - s/t + s/s_2) \\
&\quad - 2s^2/u - 3st/u - 2s - s_2 + 3st/s_2 - 2t^3/s_2u]/t \ , \\
e_4 &= 2m^2(2m^2/t + 1)^2; \qquad e_5 = -4m^2/u \ , \\
\tilde e_6 &= -16m^4/u + 2m^2(5s/u + 7t/u + 11) + t(4s/t - s/u + t/u + 17); \qquad \tilde e_7 = 2m^2 \ , \\
e_8 &= 8m^6(s/t + 2 + u/s)/su + 4(3s/t + 4 + 2s_2/s)m^4/u + 2m^2(s_2/u - 2 - t/s) \\
&\quad - (s^2/t + s + 3s_2 + t^2/s + 3tu/s)s/u; \qquad e_9 = 8(s_2 + u)/ts_2u \ , \\
e_{10} &= -4[8m^4/u + 2m^2(s/u + 2) - s_2^2/u + 4s + t + 3u]/ts_2 \ , \\
\tilde e_{11} &= 16m^6[(t+u)^2/tu + s_2/s]/s + 8m^4[(s-t)/u + t^2/su + 3(t+u)/s + u^2/st] \\
&\quad + 2m^2[u(s+u)/t + t(t+u)/s - ts_2/u - 7s_2 - 2ts_2/s - us_2/s] + (s^2 + t^2)(t+u)/u \ , \\
\tilde e_{12} &= m^2(8m^4/s - 4m^2 - s); \qquad e_{13} = m^2(8m^4/t + 4m^2 - t); \qquad \tilde e_{14} = 2m^6; \qquad e_{15} = 0 \ , \\
e_{16} &= -2[22m^2(t+u)/tu + 3t/u + 14 + u/t]/s_2 \ .
\end{aligned} \tag{B8}$$

APPENDIX C

We give here the bremsstrahlung integrals I_i appearing in Eq. (30). They are defined as

$$I_i = \frac{1}{2\pi}\int d\Omega f_i \ ; \qquad (2m)^2[\Delta]|M|^2_{2\to3} \equiv C\sum_i[\Delta]e_if_i/s_2^{n_i} \tag{C1}$$

[see (24)]. The f_i may be explicitly expressed as functions of θ_1 and θ_2 using the expressions in Appendix A. All the integrals here are four-dimensional [i.e., $\varepsilon = 0$ in (27)] and are determined using the general forms given in Ref. [2].

First we list the four basic integrals:

$$\begin{aligned}
I_6 &= \frac{2S_2}{s_2\bar y}\ln\frac{T + U - \bar y}{T + U + \bar y}, \qquad I_6' \equiv \frac{2S_2}{s_2(s+t)}\ln\frac{S_2}{m^2} \ , \\
I_8 &= \frac{4S_2}{s_2\sqrt{s}}\frac{1}{\sqrt{x_8}}\ln\frac{x_8 + s_2^2s + 2s_2\sqrt{sx_8}}{x_8 + s_2^2s - 2s_2\sqrt{sx_8}}, \qquad x_8 \equiv 4m^2(s_2s + tu) + s_2^2s \ , \\
I_{11} &= \frac{4S_2}{s_2\sqrt{stx_{11}}}\ln\frac{x_{11} + st - 2\sqrt{stx_{11}}}{x_{11} + st + 2\sqrt{stx_{11}}}, \qquad x_{11} \equiv 4m^2(s_2 - t) + st \ .
\end{aligned} \tag{C2}$$

Define

$$z_1 \equiv 2m^2s + s_2s - tu, \quad z_2 \equiv s_2u - 2m^2s - st, \quad z_3 \equiv m^2s - tu, \quad z_4 \equiv 2m^2s - tu, \quad z_5 \equiv 2m^2 + t \ . \tag{C3}$$

We may now express the remaining integrals in terms of those listed above:

$$\begin{aligned}
I_5 &= -\frac{2S_2z_4}{m^2(s+t)^3} + \frac{I_6'z_1}{(s+t)^2} \ , \\
I_9 &= \frac{1}{4S_2(s+t)^3}\{2z_1(s_2 - t)(s+t)s_2 - (z_1^2 + 2z_3S_2s)(2m^2 + s_2)\} + \frac{I_6'}{4(s+t)^2}(z_4^2 + 2m^2sz_3) \ , \\
I_{10} &= \frac{z_1}{(s+t)^2} - \frac{I_6'z_4}{2(s+t)}; \qquad I_{12} = \frac{8S_2}{m^2s_2t}\left(\frac{z_5}{x_{11}} - \frac{1}{s_2}\right) - 2I_{11}\frac{z_5(s_2 - t)}{x_{11}t} \ , \\
I_{13} &= -\frac{8S_2z_5}{x_{11}(s_2 - t)m^2t} - 2\frac{I_{11}}{t}\left(1 - \frac{s_2z_5}{x_{11}}\right) \ , \\
I_{14} &= \frac{16S_2}{stx_{11}}\left(\frac{12z_3}{x_{11}t} + \frac{\bar y^2 + s_2^2}{s_2^2m^2}\right) - \frac{4I_{11}}{x_{11}st}\left\{s_2u - sz_5 - 3z_5(s_2 - t)\frac{s}{t}\left(1 - \frac{s_2z_5}{x_{11}}\right)\right\} \ , \\
I_{15} &= \frac{s_2}{4S_2\bar y^4}\{(z_2^2 + 2S_2sz_3)(U + T) + 2\bar y^2z_2(s_2 - t)\} + \frac{I_6s_2^2}{4\bar y^4}\{(z_4 - u^2)^2 + 2m^2sz_3\} \ , \\
I_{16} &= \frac{z_2}{\bar y^2} - \frac{I_6s_2(z_4 - u^2)}{2\bar y^2} \ .
\end{aligned} \tag{C4}$$

The integrals were put into the above form using REDUCE. The integrals not listed here (including the n-dimensional ones not given in Ref. [2]) are straightforward and have been substituted directly in (30). As an aside, we point out that $x_{11}(t \leftrightarrow u)$ vanishes for $v = 1/2$, $w = w_1$. Hence one must avoid reaching *exactly* the lower bound (as for the upper) of the w integral, in numerical calculations.

[1] P. Nason, S. Dawson, and R.K. Ellis, Nucl. Phys. **B303**, 607 (1988); **B327**, 49 (1989); **B335**, 260(E) (1990).

[2] W. Beenakker, H. Kuijf, W.L. van Neerven, and J. Smith, Phys. Rev. D **40**, 54 (1989).

[3] J. Smith and W.L. van Neerven, Nucl. Phys. **B374**, 36 (1992); J.H. Kühn, E. Mirkes, and J. Steegborn, Z. Phys. C **57**, 615 (1993); M. Drees, M. Krämer, J. Zunft, and P.M. Zerwas, Phys. Lett. B **306**, 371 (1993).

[4] J.F. Gunion and H.E. Haber, Phys. Rev. D **48**, 5109 (1993).

[5] D.L. Borden, V.A. Khoze, J. Ohnemus, and W.J. Stirling, Phys. Rev. D **50**, 4499 (1994).

[6] W. Siegel, Phys. Lett. **84B**, 193 (1979).

[7] J.C. Ward, Phys. Rev. **78**, 182 (1950).

[8] A.P. Contogouris, B. Kamal, and Z. Merebashvili, Phys. Lett. B **337**, 169 (1994).

[9] A.P. Contogouris, O. Korakianitis, F. Lebessis, and Z. Merebashvili, Phys. Lett. **B344**, 370 (1995).

[10] G.A. Schuler, S. Sakakibara, and J.G. Körner, Phys. Lett. B **194**, 125 (1987); J.G. Körner and M.M. Tung, Z. Phys. C **64**, 255 (1994).

[11] I. Jack, D.R.T. Jones, and K.L. Roberts, Z. Phys. C **62**, 161 (1994); **63**, 151 (1994); M. Ciuchini, E. Franco, L. Reina, and L. Silvestrini, Nucl. Phys. **B421**, 41 (1994).

[12] G. Passarino and M. Veltman, Nucl. Phys. **B160**, 151 (1979).

[13] J. Vermaseren, *FORM User's Manual* (CAN, Amsterdam, 1991).

[14] A.C. Hearn, *REDUCE User's Manual Version 3.3* (Rand Corporation, Santa Monica, CA, 1987).

[15] R.K. Ellis, M.A. Furman, H.E. Haber, and I. Hinchliffe, Nucl. Phys. **B173**, 397 (1980).

[16] CDF Collaboration, F. Abe *et al.*, Phys. Rev. Lett. **73**, 225 (1994); Phys. Rev. D **50**, 2966 (1994).